Micromechanics-based phase-field fracture modeling of CNT-brittle matrix composites

Leonel Quinteros[a,*], Enrique García-Macías[a,b], Emilio Martínez-Pañeda[a]

[a]*Department of Civil and Environmental Engineering, Imperial College London, London SW7 2AZ, UK*
[b]*Department of Structural Mechanics and Hydraulic Engineering, University of Granada, Av. Fuentenueva sn 18002, Granada Spain*

Abstract

We present a novel micromechanics-based phase-field approach to model crack initiation and propagation in carbon nanotube (CNT) based composites. The constitutive mechanical and fracture properties of the nanocomposites are first estimated by a mean-field homogenisation approach. Inhomogeneous dispersions of CNTs are also accounted for by means of equivalent inclusions representing agglomerated CNTs. Detailed parametric analyses are presented to appraise the effect of the main micromechanical properties upon the fracture behaviour of CNT-based composites. The second step of the proposed approach incorporates the previously estimated constitutive properties into a 3D finite element based phase-field model to simulate crack initiation and propagation properties in macroscopic CNT-based composites. The effectiveness of the proposed approach is demonstrated trough three case studies, namely a single notched plate subjected to traction and shear and for a holed plate under traction loading.

Keywords: Carbon nanotubes, Composite material, Finite Element Analysis, Fracture toughness, Micromechanics, Phase-Field

1. Introduction

The development of nano-modified composite materials is crucial for futures technologies, offering a wide range of applications in structural, biomedical, electronics, automobiles, aircraft, and pipeline engineering [1]. In particular, CNT reinforced composite materials have attracted much attention due to their remarkable multifunctional properties [2–4], finding a vast variety of applications in the literature such as sensing for Structural Health Monitoring (SHM) [5, 6], design of high-strength materials [2–4], and hydrogen storage [7]. Such exceptional properties are a result of to the unique mechanical, electrical and thermochemical stability properties of CNTs [8–11]. Nevertheless, the development of reliable predictive models that can enable virtual testing of CNT reinforced components remains at early stages, particularly regarding the fracture behaviour of these composites.

In the literature, many attempts to calculate the effective elastic properties of CNTs reinforced composites have been reported using different techniques. A computationally efficient approach is offered by mean-field homogenisation methods, which allow using closed form expressions to estimate the effective elastic moduli for a wide variety of composite materials. In that regard, Hori and Nemat-Nasser [12] presented a double inclusion

*Corresponding author.
Email addresses: l.quinteros-palominos20@imperial.ac.uk (Leonel Quinteros), enriquegm@ugr.es (Enrique García-Macías), e.martinez-paneda@imperial.ac.uk (Emilio Martínez-Pañeda)

scheme (extendable for multiple inclusions) to calculate the elastic properties when an interface between the inclusion and the matrix material is accounted for. Garcías-Macías *et al.* [13] proposed an extended double inclusion method to predict the elastic properties of partially saturated composites. Wang and co-authors [14] also employed a similar approach to study the effects of the microvoids in unidirectional fiber-reinforced composites.

Successfully have been the implementation to predict crack propagation of the extended FEM (XFEM) [15], the interface finite element [16, 17] and the embedded finite element (EFEM) [18], among others. The modelling of failure mechanisms in solids based on sharp cracks may lead to complex crack topologies, costly tracking methods of discontinuities, convoluted formulations, to mention a few [19]. This situation may be overcome using a variational approach that uses a smooth variable as an interpolator between the unbroken and fully broken material states called the phase-field fracture method [20]. This method has been successfully implemented with the finite element methods (FEMs) for elastic solids [21], and it has been extended for dynamic brittle fracture [22] and for ductile materials [23]. An attractive feature of this approach for modelling cracking relates to its ability to predict crack formation and propagation without requiring adaptive mesh schemes, therefore not being necessary to know the location of the crack initiation points beforehand. Some recent application cases are in the hydrogen storage area, showing vast potential for hydrogen embrittlement [24], microscopic fracture of fibre reinforced materials [25], and reproduction of crack trajectories in functionally graded materials [26]. However, the modelling of the fracture properties of CNT reinforced composites is also a challenging task due to the difficulties involved in the estimation of the fracture energy properties. The mechanisms involved in the fracture phenomenon varies depending of the composite [27–30]. For fibre-brittle matrix system, the two main toughness contributions are the pull-out and the CNT fracture mechanism [31, 32], whose relative contributions are governed by the filler embedment length [33, 34]. Negi *et al.* [35] simulated the fracture of CNT reinforced composites by means of extended FEM (XFEM) of thin composite plates, calculating the fracture energy under the assumption of aligned straight CNTs perpendicular to the crack faces. However, the supposition of fully aligned CNTs may not be realistic. Since, in the manufacturing process of thermosetting polymers (e.g compounding and injection moulding processes), changes in the fibre orientation often occur [36–38].

There are plenty of phenomena that may considerably affect the performance of CNT-based composites [39, 40]. These may include filler waviness, agglomeration, variability in the length and direction of CNTs in the composite. Among all the previous defects, the CNTs agglomeration phenomena are difficult to avoid. The large surface area of CNTs induces strong van der Waals adhesion forces between the nanofillers, resulting in their agglomeration [41–43]. The modelling of the agglomeration using mean-homogenisation models was first explored by the two-parameter model proposed by Shi *et al.* [44], which conceives the composite as a two-phase material, including clusters or zones of agglomerated fillers and the surrounding matrix with less dispersed fillers [40]. Agglomeration has been also adressed by means of extended Halpin–Tsai (HT) models [45]. Regarding the fracture energy, only a few attempts have been made to calculate the agglomeration effects. Zeidenidi *et al.* [46] modified the fracture energy for straight CNTs, modifying the filler volume fraction through an empirical rule to be fitted by experiments.

This paper proposes a novel methodology to predict the crack propagation properties of brittle CNT reinforced composites, including the elastic and fracture constitutive energy properties utilizing a micromechanical approach. Also, a novel stochastic agglomeration model is proposed to account for inhomogeneous dispersion of CNTs

through probability distribution of the number of CNTs immerse in a bundle. Then due to the crack simulation complexity, the phase-field fracture method is implemented to predict the initiation and propagation of cracks. Then, three study cases are performed. Namely, a single-edge notched plate subjected to uniaxial loading, shear loading, and a holed plate. In which the load-displacement curves between the homogeneous dispersed CNTs and the plate with agglomerated CNTs are compared.

2. Micromechanics Modelling of CNT-reinforced composites

The structure of this section is divided in two parts. In Section 2.1, the micromechanics model used to estimate the elastic tensor is presented, while Section 2.2 gives the micromechanics basis to compute the fracture energy of CNT based composites.

2.1. Effective elastic properties

2.1.1. Effective elastic moduli using a double-inclusion model

To estimate the elastic properties a micromechanical model is developed, including the matrix, the particle inclusions, and the interface between them, which are denoted by indexes m, p, and i, respectively. Let V be the representative volume element (RVE) of a matrix doped with CNTs as shown in Fig. 1. This RVE must contain a sufficient number of fillers such that the overall properties of the composite are statistically represented. A local system coordinate $\mathrm{K}' \equiv \left\{0; x_1' x_2' x_3'\right\}$ is fixed at each particle and two Euler angles, θ and γ, are defined to describe the relative orientation of the filler with respect to the global coordinate system. The geometrical dimensions of the CNTs are assumed constant throughout the RVE, including their length L_{cnt}, diameter D_{cnt}, and the interphase thickness t. Following the notation of Hori and Nemat-Nasser [12], a CNT and its surrounding interphase is

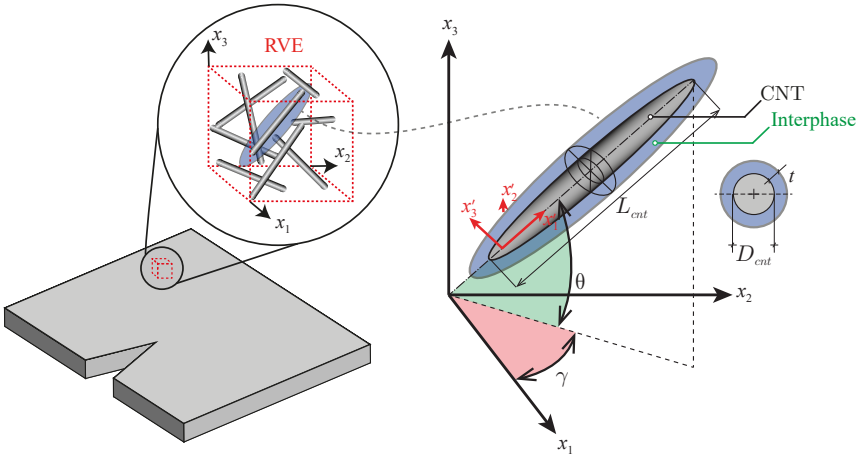

Figure 1: Schematic representation of a CNT-based composite plate, RVE, and local orientation of a CNT defined by the Euler angles, θ and γ.

modelled as a double inclusion as shown in Fig. 1. Using the linear elastic tensors of the constituent phases, $\mathbf{C}_m$, $\mathbf{C}_p$, and $\mathbf{C}_i$, and the corresponding volume fractions as f_m, f_p and f_i, the effective contitutive tensor of the three-phase composite can be obtained as [13, 47]:

$$\bar{\mathbf{C}} = (f_m\mathbf{C}_m + f_i\langle\mathbf{C}_i : \mathbf{A}_i\rangle + f_p\langle\mathbf{C}_p : \mathbf{A}_p\rangle) : (f_m\mathbf{I} + f_i\langle\mathbf{A}_i\rangle + f_p\langle\mathbf{A}_p\rangle)^{-1}, \tag{1}$$

where $\mathbf{I}$ is the fourth-order identity tensor, whereas $\mathbf{A}_i$ and $\mathbf{A}_p$ refers to the concentration tensors for the interphases and the inclusions, respectively, which can be written as a function of the dilute concentration tensors $\mathbf{A}_i^{dil}$ and $\mathbf{A}_p^{dil}$ [12] as:

$$\mathbf{A}_\chi = \mathbf{A}_\chi^{dil} : (f_m\mathbf{I} + f_i\mathbf{A}_i^{dil} + f_p\mathbf{A}_p^{dil})^{-1}, \quad \chi = p, i \tag{2}$$

where,

$$\mathbf{A}_\chi^{dil} = \mathbf{I} + \mathbf{S} : \mathbf{T}_\chi, \quad \chi = p, i \tag{3}$$

$$\mathbf{T}_\chi = -(\mathbf{S} + \mathbf{M}_\chi)^{-1}, \quad \chi = p, i \tag{4}$$

$$\mathbf{M}_\chi = (\mathbf{C}_\chi - \mathbf{C}_m)^{-1} : \mathbf{C}_m, \quad \chi = p, i \tag{5}$$

Tensor $\mathbf{S}$ in Eqs. (3) and (4) correspond to the Eshelby's tensor for an spheroidal particle, determined by the aspect ratio $\kappa = L_{cnt}/D_{cnt}$ and the matrix's Poisson ratio, ν_m.

The angle brackets $\langle\cdot\rangle$ in Eq. 1 denote the orientational average over the Euler space weighted by an orientation distribution function (Ω), Specifically, the orientational average of a certain function F reads:

$$\langle F \rangle = \int_0^{2\pi}\int_0^{\pi/2} F(\gamma,\theta)\Omega(\gamma,\theta)\sin(\theta)\mathrm{d}\theta\mathrm{d}\gamma, \tag{6}$$

the particular case of random filler orientations, the orientation distribution function takes a constant value $\Omega(\gamma,\theta) = 1/2\pi$.

Note that for soft interphases, the intherphase valume fraction f_i can be calculated using the formulae derived by Xu *et al.* [48] as,

$$f_i = (1-f_p)\left(1 - \exp\left\{-\frac{6f_p}{1-f_p}\left[\frac{\eta}{n(\kappa)} + \left(2 + \frac{3f_p}{n^2(\kappa)(1-f_p)}\right)\eta^2 + \frac{4}{3}\left(1 + \frac{3f_p}{n(\kappa)(1-f_p)}\right)\eta^3\right]\right\}\right), \tag{7}$$

with η being the ratio of the interfacial thickness t and the equivalent diameter D_{eq} (i.e. $\eta = t/D_{eq}$). The equivalent diameter denotes the diameter of an equivalent sphere with the same volume as the particles [49] and, in the case of CNTs, with aspect ratio $k > 1$, it can be determined as $D_{eq} = D_{cnt}\kappa^{1/3}$. Finally, the term $n(\kappa)$, denotes the sphericity of the CNTs, and it is defined as the ratio of the surface area between the equivalent sphere and that of the particles, which is:

$$n(\kappa) = \frac{2\kappa^{2/3}\tan\varphi}{\tan\varphi + \kappa^2\varphi}, \tag{8}$$

with $\varphi = \arccos(\beta)$, and $\beta = 1/\kappa$.

2.1.2. Agglomeration of CNTs

In order to incorporate agglomeration effects into a mean-field homogenization framework, Shi *et al.* [44] developed a two parameter model distinguishing the filler concentration in bundles and matrix. The entire volume of the RVE, V, and the volume of CNTs V_r can be written as:

$$V = V_{bundles} + V_{matrix}, \quad V_r = V_r^{bundles} + V_r^m, \tag{9}$$

where $V_{bundles}$ and V_{matrix} refer to the volume of the bundles and the matrix, respectively, whereas $V_r^{bundles}$ and V_r^{matrix} stand for the CNT concentration in the bundles and in the matrix, respectively. Now, two parameters, χ and ζ, can be defined as follows:

$$\chi = \frac{V_{bundles}}{V}, \quad \zeta = \frac{V_r^{bundles}}{V_r}, \tag{10}$$

thus, defining $f_p = V_r/V$ as the total CNTs volume fraction, the filler concentrations in the bundles f_{bundle} and in the matrix f_{matrix} can be obtained as:

$$f_{bundles} = \frac{V_r^{bundles}}{V_{bundles}} = \frac{\zeta}{\chi} f_p, \quad f_{matrix} = \frac{V_r^{matrix}}{V_{matrix}} = \frac{1-\zeta}{1-\chi} f_p. \tag{11}$$

A two step homogenisation model inspired by reference [13], is implemented as sketched in Fig. 2. The first step consists in the estimation of the effective properties of the clusters and the homogeneously dispersed CNTs in the surrounding matrix independently. To do so, the double-inclusion model of Eq. 1 is applied considering spheroidal bundles. The resulting constitutive tensors are denoted by $\bar{\mathbf{C}}_m$, which is the phase with CNTs homogeneously dispersed in the matrix, and $\bar{\mathbf{C}}_b$ is the CNTs bundles. Then, the the overall constitutive tensor of the composite is obtained by applying the two-phase Mori-Tanaka [50] as,

$$\bar{\mathbf{C}} = \bar{\mathbf{C}}_m + \chi(\bar{\mathbf{C}}_b - \bar{\mathbf{C}}_m) : \mathbf{A}, \tag{12}$$

where,

$$\mathbf{A} = \mathbf{A}_{dil} : ((1-\chi)\mathbf{I} + \chi \mathbf{A}_{dil})^{-1}, \tag{13}$$

and

$$\mathbf{A}_{dil} = (\mathbf{I} + \mathbf{S} : \mathbf{C}_m^{-1}) : (\mathbf{C}_b - \mathbf{C}_m)^{-1}. \tag{14}$$

The Eshelby's tensor in Eq. 14 depends upon the geometry of the clusters, which, as mentioned earlier, are assumed to be spheroidal. is important to note that the volume fraction of the bundles is given by the parameter χ.

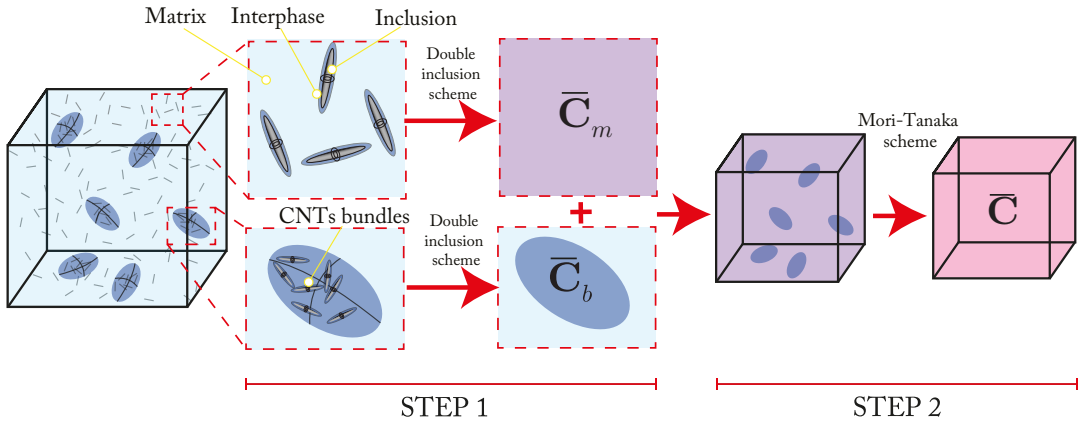

Figure 2: Scheme of the two step micromechanics model to incorporate CNT agglomeration effects.

2.2. *Fracture energy formulation*

2.2.1. *Fracture Energy: pull-out and fracture*

The fracture in CNT-based composites occurs in two stages. The first, in which matrix fracture energy G_0 is reached, and then, the energy increase due to the bridging effect granted by the fibres. The critical fracture energy G_c can be obtained by adding to the matrix fracture energy G_0 the two main toughening mechanisms considered in the literature [33, 51], the fracture of CNTs and the CNTs pull-out, as:

$$G_c = G_0 + G_{PF}, \tag{15}$$

where G_{PF} is the fracture energy contributions given by the CNT pull-out and CNT fracture, sketched in Fig. 3(a).

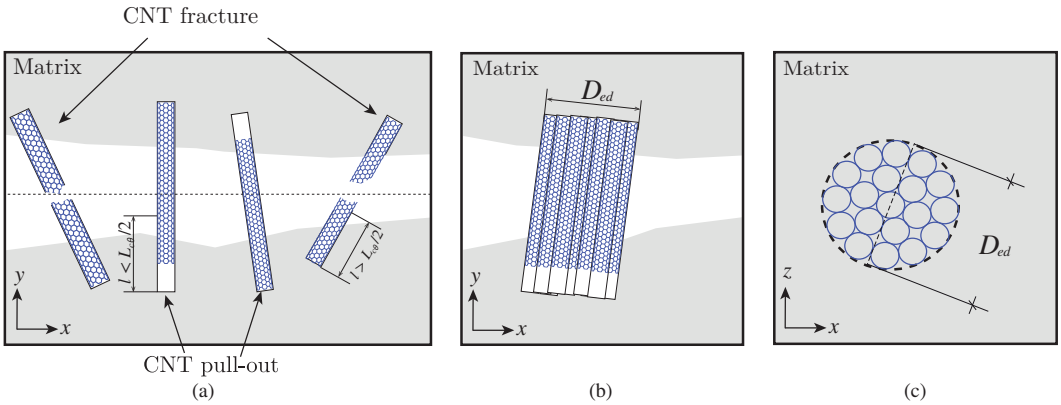

Figure 3: Scheme of the CNT-induced bridging mechanism (a) CNT pull-out and CNT rupture mechanism (b) Agglomeration model (c) Cross-section plane of the agglomeration model.

The critical length $L_{c\theta}$ [33, 51] is a threshold value that allows to differentiate between both mechanisms. That length can be obtained from a force balance in a CNT as [52]:

$$A_{cnt}\sigma_{ult\theta} = P_{cnt}l\tau_{int}e^{\mu\theta}. \tag{16}$$

where l is the CNT embedded length, A_{cnt} is the area of the CNT cross-section, P_{cnt} is the perimeter of the cross-section, τ_{int} is the interfacial frictional shear stress, and $\sigma_{ult\theta}$ is the fracture stress of oblique fibres. For brittle fibres $\sigma_{ult\theta}$ is given by [53]:

$$\sigma_{ult\theta} = \sigma_{ult}(1 - A\tan(\theta)), \tag{17}$$

where σ_{ult} is the fracture stress of a CNT, and A is a constant determining the fibre inclined strength. Then, if the CNT length is lower than $l = L_{c\theta}/2$, the CNT will pull out, else the CNT rupture mechanism will take place. To calculate the fracture energy the work done W of a single CNT under pull-out and fracture is estimated as [33],

$$W(l,\theta) = \begin{cases} l^2\tau_{int}P_{cnt}\exp(\mu\theta)/2 & \text{if } l < \frac{L_{c\theta}}{2} \\ A_{cnt}\sigma_{ult}^2 L_{cnt}/\left(2E_{cnt}\right) & \text{if } l \geq \frac{L_{c\theta}}{2} \end{cases}, \tag{18}$$

in which L_{cnt} is the CNT length, E_{cnt} is the Young's modulus, and μ is the snubbing friction coefficient for misaligned CNTs [52]. Then, the fracture energy for a constant CNT length L_{cnt}, without supposing any shape of the CNT, can be obtained as [32],

$$G_{PF} = \frac{2f_p}{A_{cnt}L_{cnt}}\int_{\theta=0}^{\pi/2}\int_{l=0}^{L_{cnt}/2}\cos(\theta)W(l,\theta)g(\theta)\mathrm{d}l\mathrm{d}\theta, \tag{19}$$

where $g(\theta)$ is the orientation distribution, defined in the next section. Eqs. (18) and (19) are commonly developed supposing that the CNTs has cylindrical shape, then $A_{cnt} = \pi D_{cnt}^2/4$ and $P_{cnt} = \pi D_{cnt}$.

2.2.2. CNTs orientation dependency

During the manufacture of CNT-reinforced composites, CNTs can be oriented in multiples directions. Although the orientation of CNTs is three-dimensional in nature, just one angle θ between the loading direction and the fibre axis suffices to capture the effect of the fibre orientation in short-fibre composites [51, 54]. In statistical terms, a PDF $g(\theta)$ can be defined to describe the planar orientation distribution of the CNTs as [55, 56]:

$$g(\theta) = \frac{\sin(\theta)^{2p-1}\cos(\theta)^{2q-1}}{\int_{\theta_{min}}^{\theta_{max}}\left[\sin(\theta)^{2p-1}\cos(\theta)^{2q-1}\right]\mathrm{d}\theta}, \tag{20}$$

The orientation angle θ spans between θ_{min} and θ_{max}, which are the minimum and maximum CNT inclinations with respect to the load direction, while $p \geq 1/2$ and $q \geq 1/2$ are shape parameters that determine the shape of the PDF (see ref. [51]).

2.2.3. CNT agglomeration effects

The previous formulation assumes well-dispersed CNTs. However, as discussed in Section 2.1.2, CNTs tend to agglomerate in bundles, with the subsequent detrimental effect upon the fracture toughness [30, 57]. In order to include such an effect, a new agglomeration formulation is proposed in this work. Since no assumptions about the filler shape have been made in Eqs. (18) and (19), the CNT agglomeration will be estimated from the cross-section properties. The number of CNT with diameter D_{cnt} immerse in the bundle controls its cross-section, so in this work will be assumed that the bundle cross-section is constituted of smaller CNTs of diameter D_{cnt} packed in a bigger circle of diameter D_{ed} as sketched in Fig. 3(b), following the so-called "equal circles packed in circle problem" [58] pattern as sketched in Fig. 3(c) for 19 circles. The perimeter of the CNT bundle is approximated to the perimeter of the enclosing circle diameter D_{ed}, while the bundle cross-section area is the area of a single CNT multiplied by the number of N CNTs immerse in it. Some examples values of the equal circles packed in circle problem are shown in Table 1, the ratio is defined as $R = D_{ed}/D_{cnt}$, while the density is expressed as $\rho_A = (NA_{cnt})/A_{ed}$, where A_{ed} is the enclosing circle area.

Table 1: Ratio and density in function of the number of CNTs inside the enclosing circle diameter

Number of CNTs N	**Ratio** $R = D_{ed}/D_{cnt}$	**Density** $\rho_A = (NA_{cnt})/A_{ed}$
1	1	1
2	2	0.5
5	2.701	0.685
10	3.813	0.687
20	5.122	0.762
50	7.947	0.791
100	11.0821	0.8142

The approximated agglomerated perimeter function $P_{agg}(N, D_{cnt})$ is defined as $P_{agg}(N, D_{cnt}) = \pi(D_{ed}) = \pi(RD_{cnt})$, and the area as a function of the number CNTs inmerse in the agglomeration $A_{agg}(N, D_{cnt})$ can be calculated as $A_{agg}(N, A_{cnt}) = NA_{cnt}$. Now, with the functions $P_{agg}(N, D_{cnt})$ and $A_{agg}(N, A_{cnt})$ well defined from the data of Table. 1 (see ref. [58]), the fracture energy for agglomerated CNTs can be estimated as,

$$G_{PFN}^{agg}(N) = \frac{2f_p}{A_{agg}(N, A_{cnt})L} \int_{\theta=0}^{\pi/2} \int_{l=0}^{L/2} \cos(\theta) W(l, \theta, N) g(\theta) \mathrm{d}l\mathrm{d}\theta, \tag{21}$$

with, $W(l, \theta, N))$ defined as,

$$W(l, \theta, N) = \begin{cases} l^2 \tau_{int} P_{agg}(N, D_{cnt}) \exp(\mu\theta)/2 & \text{if } l < \frac{L_{c\theta}}{2} \\ A_{agg}(N, A_{cnt}) \sigma_{ult}^2 L / (2E_{cnt}) & \text{if } l \geq \frac{L_{c\theta}}{2} \end{cases}. \tag{22}$$

It is worth notice that the fracture energy for agglomerated CNTs is the same as the fracture energy for a single CNT since the area is simplified from the Eqs. (22) and (21). So, the only important mechanism is the CNT pull-out. Another important assumption is that the critical length $L_{c\theta}$ will be the same as the critical length for a

single CNTs. Since the CNTs are not unified as a big CNT, the force balance of Eq. (17) on each CNT will remain the same. So, the inhomogenities would not change the length which distinguish between the CNT pull-out and the CNT fracture on CNTs that constitutes it.

In order to simulate the randomness in the number of fillers clustered in the agglomerates, the number of CNTs N will be defined in statistical terms through a Weibull PDF $p(D)$ with parameters λ and k. On this basis, the CNTs fracture can be estimated by integrating G_{PFN}^{agg} weighted by $p(N)$ between N_{min} and N_{max} as,

$$G_{PF}^{agg} = \int_{N_{min}}^{N_{max}} G_{PFN}^{agg} p(N) \mathrm{dN} \tag{23}$$

The shape parameters λ and k can be calculated numerically given the mean of the N_μ and the standard deviation N_σ. The two-parameter agglomeration approach previously presented in Section 2.1.2 is also introduced here. To do so, the classical rule of mixtures is used to combine the contributions of agglomerated and the well dispersed CNTs, leading to:

$$G_c = G_{I0} + (1-\zeta) G_{PF}(f_p) + \zeta G_{PF}^{agg}(f_p), \tag{24}$$

where G_{PF} and G_{PF}^{agg} are the fracture energy contributions of uniformly dispersed and agglomerated CNTs, respectively. Note that the formulation in Eq. (24) only depends on ζ. This is due to the linearity between the volume fraction and the fracture energy in Eq. (21).

3. Phase-field fracture method applied to brittle materials

Consider a solid domain Ω which includes a discontinuous surface Γ. To characterises a discrete crack an auxiliary field variable field ϕ is defined that takes values from $\phi = 0$ to $\phi = 1$, which correspond to intact and fully broken state of the material, respectively. From a continuum mechanics approach, variable ϕ describes the development of micro-cracks and micro-voids. The size of the regularised crack surface is dominated by the length scale parameter ℓ. The selection of a suitable value ℓ determines the accuracy of the simulation; it must not depend on the size of mesh elements [21] nor affect the material strength [25]. The fracture energy can be approximated as,

$$\int_\Gamma G_c \mathrm{d}\Gamma \approx \int_\Omega G_c \Gamma_\ell(\ell, \phi) \mathrm{d}\Omega = \int_\Omega G_c \left(\frac{1}{2\ell}\phi^2 + \frac{\ell}{2} |\nabla \phi|^2 \right) \mathrm{d}\Omega \tag{25}$$

where G_c is the critical energy release rate. Then, taking the integration over the boding and including the phase-field contribution, the following expression Ψ is obtained ,

$$\Psi = \int_\Omega \left(g(\phi)\psi_0 + G_c \left(\frac{1}{2\ell}\phi^2 + \frac{\ell}{2} |\nabla \phi|^2 \right) \right) \mathrm{d}\Omega \tag{26}$$

in which ψ_0 is the strain energy density of the undamaged solid and the term $g(\phi) = (1-\phi)^2 + k$ describes the degradation of the stored energy with evolving damage. The parameter k is chosen to be small as possible to keep the system of equations well-conditions; $k = 1 \times 10^7$ will be employed throughout this work.

Then, applying Gauss theorem in (26), the coupled system to be solve is,

$$\begin{aligned} g(\phi) \nabla \cdot \boldsymbol{\sigma} = 0 \quad &\text{in} \quad \Omega \\ G_c \left(\frac{1}{\ell}\phi - \ell \Delta \phi \right) - 2(1-\phi)\psi_0 = 0 \quad &\text{in} \quad \Omega \end{aligned} \tag{27}$$

Here, $\boldsymbol{\sigma}$ denotes the Cauchy stress tensor.

4. Results and discussion

In the subsequent analyses, we asses the potential of the proposed micromechanics-based phase-field approach are for predicting the fracture behaviour of epoxy doped with multiwalled carbon nanotubes (MWCNTs). The material parameters, which are kept constant throughout the study, are reported in Table 2. For better illustration, this section is divided into two parts. In the first place, the effective properties of CNT-reinforced composites computed by the micromechanics method from Section 2 are discussed in Section 4.1. Section 4.2 reports the macroscopic crack propagation analyses of three different case studies.

Table 2: Micromechanical variables of MWCNT/epoxy composites. Taken from refs. [59] and [33].

Name	Symbol	Value
Length of CNTs	L_{cnt}	3.21 μm
Outer diameter of CNTs	D_{cnt}	10.35 nm
CNT volume fraction	f_{cnt}	1 %
Elastic modulus of CNTs	E_{cnt}	700 GPa
Elastic modulus of epoxy	E_m	2.5 GPa
Possion's ratio of CNTs	ν_{cnt}	0.3
Possion's ratio of epoxy	ν_m	0.28
Interphase thickness	t	31.00 nm
Elastic modulus of interphase	E_i	2.17 GPa
Strength of CNTs	σ_{cnt}	35 GPa
Agglomeration parameter χ	χ	0.2
Agglomeration parameter ζ	ζ	0.4
Interfacial shear strength	τ_{cnt}	47 MPa
Experimental orientation limit angle	A	0.083
Fracture energy of unmodified epoxy	G_{matrix}	133 J/m^2
PDF Mean value of the number of CNT in the agglomeration	N_μ	10
PDF Standard deviation of the number of CNT in the agglomeration	N_σ	$0.1N_\mu$
Minimum number of CNTs in the agglomeration	N_{Min}	1
Maximum number of CNTs in the agglomeration	N_{Max}	50
Minimum CNT orientation angle	θ_{min}	0
Maximum CNT orientation angle	θ_{max}	$\pi/2$

4.1. Effective mechanical properties of CNT-reinforced composites

4.1.1. Uniformly dispersed CNTs

The mechanical properties of composites doped with uniformly dispersed CNTs are first studied. Figure 4(a) depicts the effective Young's modulus as a function of the filler aspect ratio L_{cnt}/D_{cnt}, for different CNT volume fractions. The Young's modulus exhibits a slight increase at low filler aspect ratios although it tends to converge a stable value for moderate to large aspect ratios ($L_{cnt}/D_{cnt} \geq 400$). It is noted in this figure the leading role of the CNT volume content upon the effective elastic modulus of the composite. For instance, it is found that the addition of only 0.5% volume fraction of CNTs leads to an increase of around 20% of the elastic modulus of pristine epoxy.

The fracture energy exhibits instead a more complicated behaviour. Firstly, the effect of filler orientation upon the fracture energy is investigated in Fig.4(b). This figure shows fracture energy G_c as a function of the

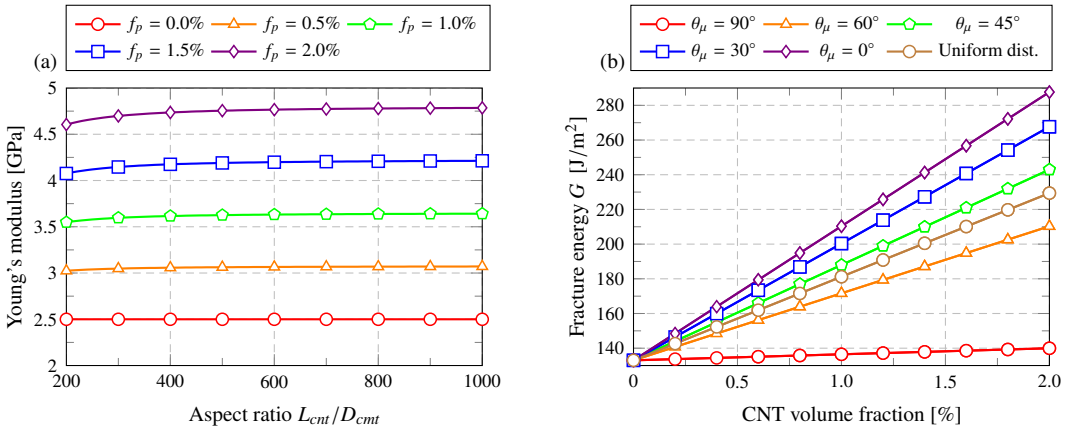

Figure 4: Effective elastic modulus of MWCNT-reinforced composites as a function of the CNT aspect ratio L_{cnt}/D_{cnt} for different filler volume fractions and assuming uniformly dispersed CNTs (a). Fracture energy of MWCNT-reinforced composites as a function of the filler aspect ratio L_{cnt}/D_{cnt}, considering different CNT contents (b).

filler volume fraction, changing the CNT mean angle direction θ_μ of the distribution. The parameters p and q are obtained for a fixed standard deviation $\theta_\sigma = 0.05\frac{\pi}{2}$, increasing mean values θ_μ from 0° to 90° and a random distribution fixing $p = q = 1/2$. It is observed that all the cases approximately follow a linear relationship with the CNT volume fraction. It is also noted that filler misalignment diminishes the fracture energy.

In Figure 5(a) reports the effects of the filler aspect ratio and the filler volume content upon the fracture energy of CNT-based composites, assuming random CNTs orientation. Note that all the curves increase until a particular aspect ratio around 370 is reached. On those curves, firstly the CNT pull-out contribution dominates the fracture behaviour, and then, the rupture mechanism does. Figure 5(b) depicts the fracture energy as a function of the aspect ratio for different CNT mean angle θ_μ. The critical aspect ratio increase when the CNTs are aligned with the load.

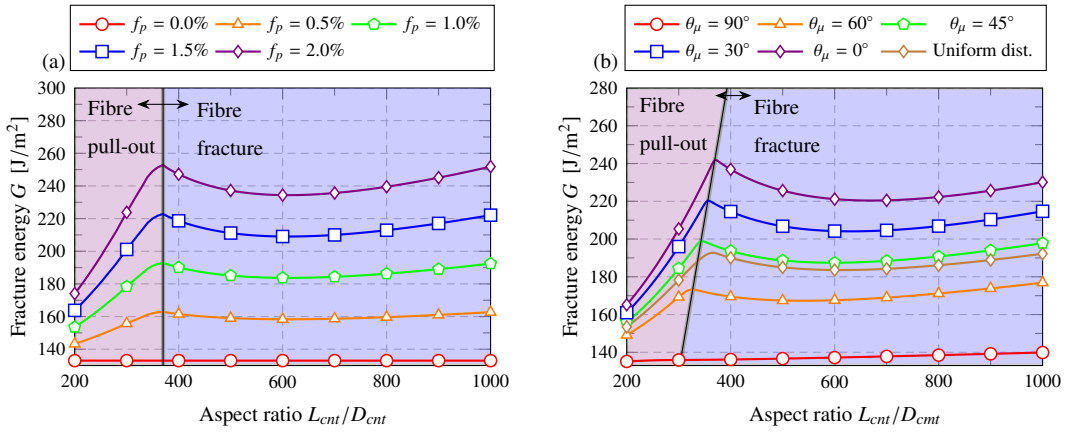

Figure 5: Fracture energy of MWCNT-reinforced composites as a function of the filler aspect ratio L_{cnt}/D_{cnt}. Considering different CNT filler content (a). Considering different CNT orientation distributions (b).

4.1.2. Inhomogeneous CNT dispersions

This section assesses the theoretical approach proposed for the modelling of filler agglomeration effects upon the elastic moduli and fracture energy of CNT-based composites. The same parameters of Table. 2 are adopted throughout this section.

Fig. 6(a) presents the Young's modulus as a function of the CNT filler volume fraction for different values of the agglomeration parameter ζ. It is noted that all the curves start at 2.5 GPa, which is the value for the Young's modulus of pristine epoxy. If the agglomeration parameter ζ increases, the curve will have a lower slope. In that case, the CNTs volume fraction goes from a uniformly dispersed matrix to concentrate all the CNTs in bundles generating discontinuities in the materials, losing the general stiffness. Figure 6(b) depicts the elastic modulus as function of the filler aspect ratio, considering different volume fractions. This Figure is identical to the Figure presented in Fig. 4(a), however the Young's modulus values is substantially lower due to the effect of the CNTs inhomogeneities. The effect of the filler aspect ratio is almost negligible because it just affects the specific range of aspect ratios between 200 and 400. After that interval, the Young's modulus exhibits a constant trend.

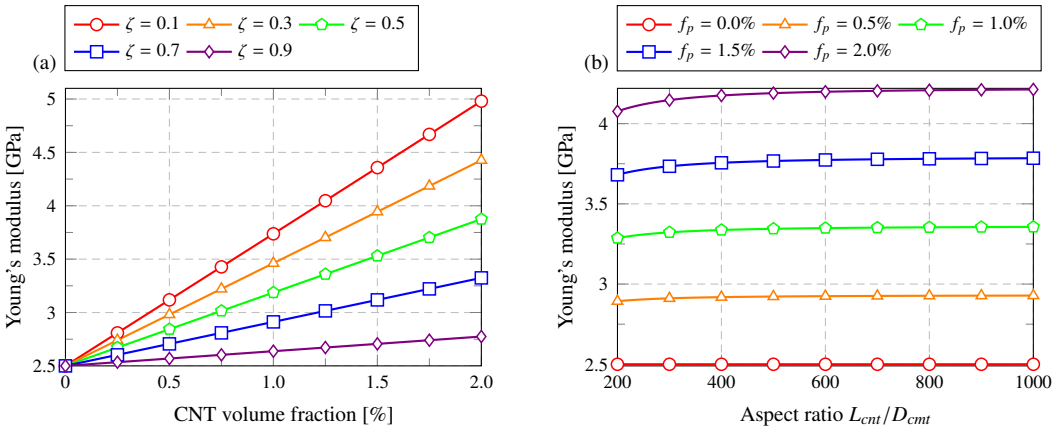

Figure 6: Estimation of the effective elastic modulus of MWCNT-reinforced composites as a function of the volume fraction, and considering the diameter based agglomeration model. The effect of the agglomeration parameter ζ, is assessed for a constant value of $\chi = 0.2$ (a). Young's modulus as a function of the aspect ratio L_{cnt}/D_{cnt} for different volume fraction f_p values.

The effect of the filler agglomeration upon the fracture energy is investigated in Figs. 7 and 8. The mean number of CNTs in a bundle N_μ is a crucial factor as highlighted in Fig. 7. The case $N_\mu = 1$ corresponds to the case of an homogeneous dispersion of CNTs. It is clear in Fig. 7 that increasing N_μ (i.e. more severe agglomeration) substantially decreases the effective fracture energy of the composite in the filler aspect ratios dominated by the pull-out mechanism. This is due to the increase of the cross-section of the equivalent agglomerated fillers in Eq. (22). Nevertheless, the detrimental effects of agglomeration decreases as the filler aspect ratio increases, tending to a common slope from an aspect ratio of 800. This is due to the effect of the fracture energy induced by fibre fracture in Eq. (22), which is proportional to the number of CNTs, which keep constant the trend in the fibre fracture domain section of the fracture energy. It is important to remark that, in these cases, some of the phenomena related to filler agglomeration and reported from experimentation that are not considered herein may play a leading effect. These include the formation of microcracks due to stress concentrations as reported

in reference [60], which considerably reduce the energy contribution of CNT fracture. Such effects are hardly conceivable within a mean-field homogenization approach, and atomistic simulations accounting for the local interaction between the filler and the matrix phases becomes imperative. Nevertheless, given that the aspect ratios of CNTs are typically below 1000, the presented approach is assumed accurate for the aim of the present work.

The effect of the agglomeration parameter ζ is shown on the fracture energy is illustrated in Fig. 8(a), considering different aspect ratio. The curves goes from uniformly dispersed CNTs ($\zeta = 0.1$) to highly agglomerated CNTs($\zeta = 0.9$) reducing dramatically the fracture energy due to the high number of inhomogeneities. Finally, Fig. 8(b) presents the fracture energy as function of the aspect ratio, considering different filler volume fraction. The same plot was shown in the Fig. 5(a) for uniformly dispersed CNTs, however the values as slightly lower due to the incorporation of agglomerations parameter based on a choice of $\zeta = 0.4$.

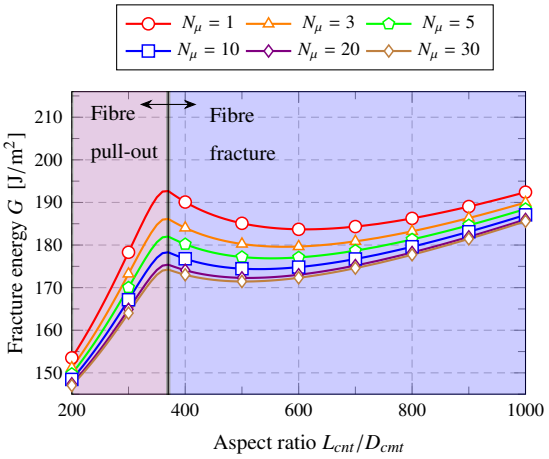

Figure 7: Estimation of the fracture energy of MWCNT-reinforced composites as function of the filler aspect ratio, considering different number of CNTs agglomerated in bundles N_μ in the proposed agglomeration model.

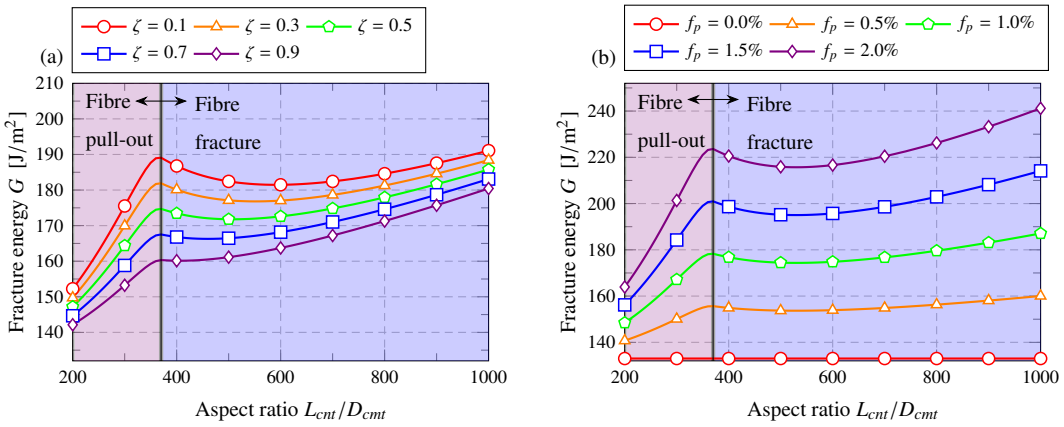

Figure 8: Estimation of the fracture energy as function of the aspect ratio in a MWCNT-reinforced composites, considering different values ζ (a). filler volume fractions (b).

4.2. Case studies of macroscopic crack propagation

In this section, three case studies sketched in Fig. 9 are reported, namely a single-edge notched plate subjected to uni-axial loading, shear loading and a holed plate. These studies are carried out using the same parameters in

Table 2. Load-displacement curves are obtained considering both homogeneous and inhomogeneous dispersion of CNTs, as well as different CNT volume fractions.

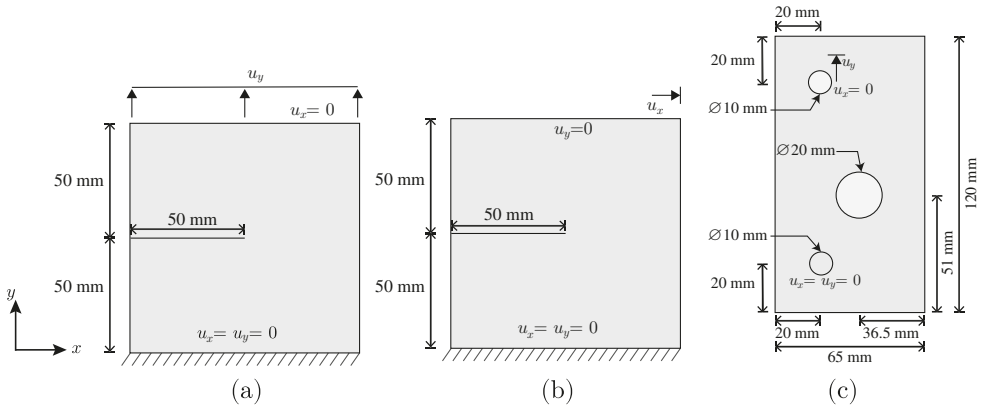

Figure 9: Geometry and boundary condition of the (a) plate in traction, (b) plate under shear, and (c) the holed plate.

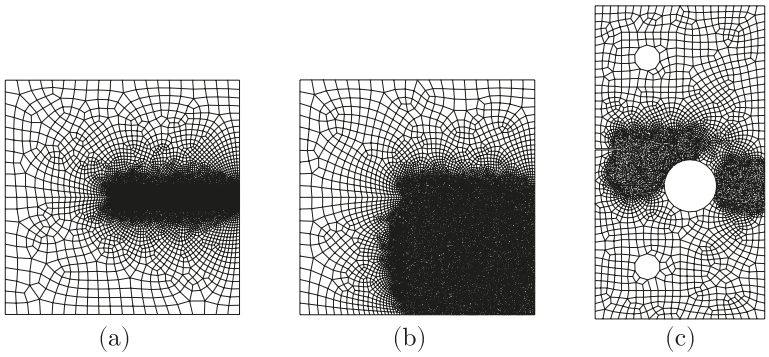

Figure 10: Mesh of the (a) plate in traction, (b) plate under shear, and (c) the holed plate.

4.2.1. Single-edge notched specimen subjected to uniaxial tension

The geometry, dimensions and boundary conditions of the first case study are presented in Fig. 9(a). It consists of a 10 cm square plate notched on the left side and subjected to traction displacements in the upper edge while pinned in the lower edge. The mesh of the plate is shown in Fig. 10(a). It includes 8532 four nodes plane strain elements. A refinement was made in the expected crack propagation zone. The length scale ℓ in was chosen as $h < \ell/7$ to ensure mesh independency [21].

Figure 12(a) presents the load-displacement curves obtained considering different CNT volume fractions for well-dispersed CNTs, whereas Fig. 12(a) accounts for agglomeration effects. In both cases, the force-displacement curves rise linearly until a critical load is reached in which the fracture has an unstable behaviour. In Both cases, maximum displacements are found in a narrow interval between 0.115 mm and 0.12 mm. The maximum value achieved by the composite plate doped with uniformly dispersed CNTs is 2.72 kN, which is 11.5% bigger than the one found considering filler agglomeration.

The crack pattern of the plate for two different time instants in Fig. 11. The phase field variable ϕ varies from 0 (blue) to 1 (red), which correspond to intact and fully cracked conditions, respectively. In this case, the material parameters are taken from Table 2, assuming uniformly disperse CNTs at a volume content of 1%.

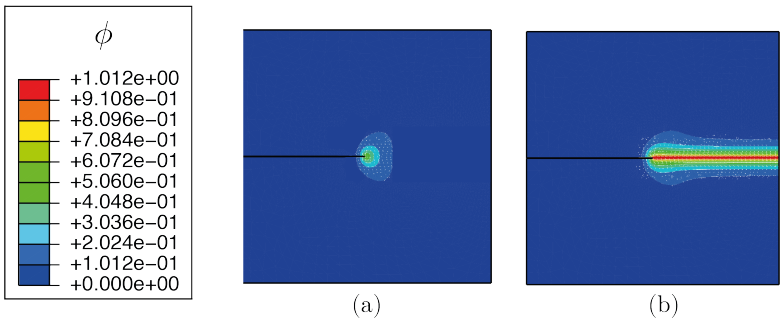

Figure 11: Phase field contours plots (ϕ) of a square notched plate subjected to an increasing uniaxial load at displacement values of (a) u_y = 0.1168 mm and (b) u_y = 0.117 mm. It is assumed a volume fraction of 1% of uniformly dispersed CNTs.

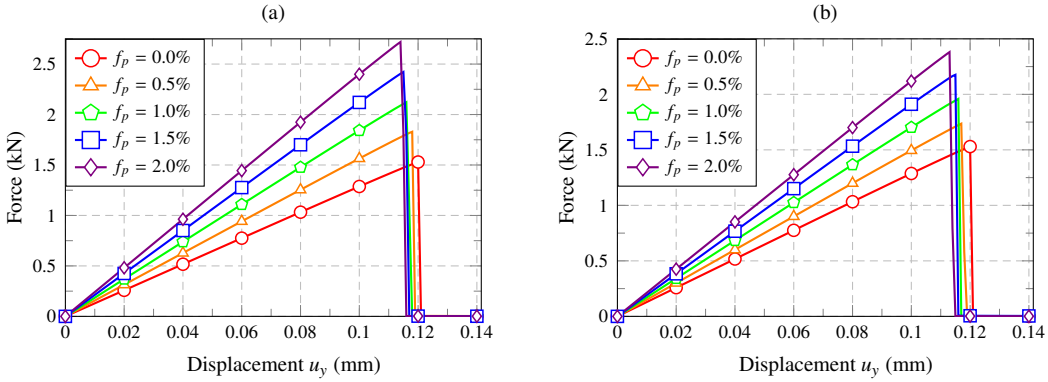

Figure 12: Load displacement curves considering different filler volume fraction for uniformly dispersed (a) and agglomerated CNTs (b). For the inhomogeneous case the parameters shown in Table. 2.

4.2.2. Notched specimen under shear loading

The same plate shown in the previous section is herein subjected to shear loading applied at the top edge. The geometric considerations and the boundary conditions are given in Fig. 9(b). Its corresponding mesh is shown in Fig. 10(b), which has 19318 elements and has an element refinement in the area where the crack is expected to grow. The parameter length scale employed for the phase field fracture method is chosen as $h < \ell/5$.

Phase field contours are shown in Fig. 13 for four stages of the crack of the previosly described plate, with applied horizontal displacements of u_x=0.165 mm. A displacement of u_x = 0.169 mm provokes a small damaged area near the crack tip, followed by the propagation of a diagonal crack through the material towards the left bottom corner.

The load-displacement curves of the second study case are shown in Fig. 14(a) and Fig. 14(b) for uniformly dispersed and non-uniformly dispersed CNTs,respectively. Those figures shows similar behaviour as the previously presented, higher volume fractions allow the material to support larger forces and energy. The shear force applied to the plate reach a peak related to the crack growth, when the plate lose stiffness to unstable crack in the narrow displacement interval of 0.265 mm and 0.28 mm for both curves. Note that CNTs agglomeration contributes to a reduction of the maximum force sustained by the doped plate, e.g for a CNT filler volume fraction of 2% the reduction was about 14.3%. It is also noted that the unstable crack appears at slightly larger displacements for higher CNT volume fractions.

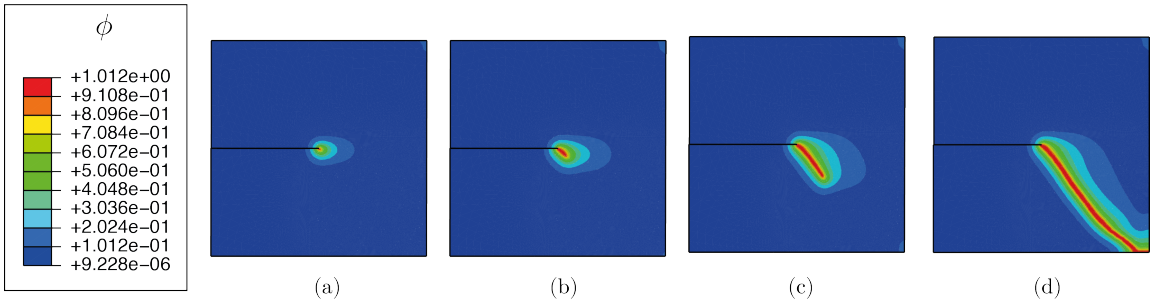

Figure 13: Phase field contour plots (ϕ) for horizontal top displacements of (a) u_x = 0.165 mm, (b) u_x = 0.195 mm, (c) u_x = 0.21 mm, and (d) u_x = 0.283 mm. It is assumed a volume fraction of 1% of uniformly dispersed CNTs.

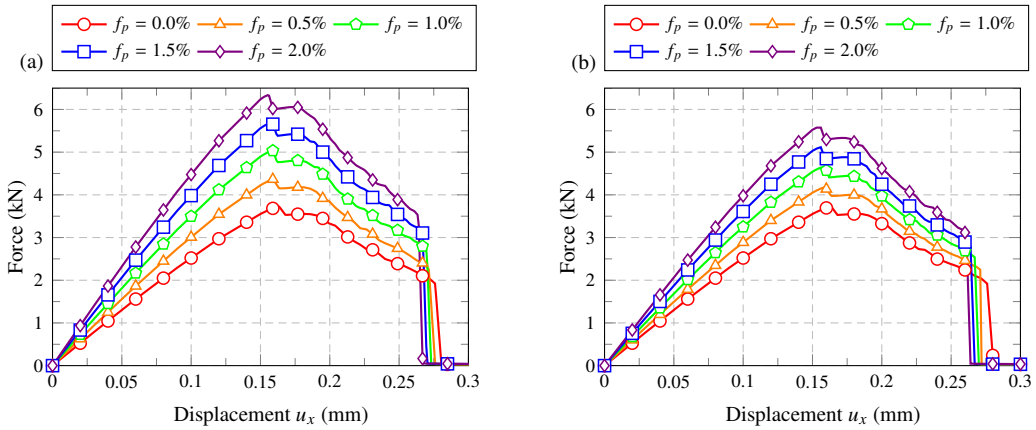

Figure 14: Notched specimen subjected to shear load displacement curve trough volume fractions, for well-dispersed (a) and agglomerated CNTs (b). For the inhomogeneous case the parameters shown in Table. 2.

4.2.3. Holed plate under traction loading

The third case study is a holed plate with geometry and boundary conditions shown in Fig. 9(c). In this case study, the loading is applied through displacement controlled metal pins inserted into the two 10 mm diameter holes. The FEM mesh of this case study is shown in Fig. 10(c), which contains 9301 elements. The length scale is set to $h < \ell/2.5$. The crack contour is shown in Fig. 15, which exhibits four stages. In Fig. 15(a) a small phase field value ϕ is concentrated at the notch tip. Then, the crack propagates, reaching the centre's hole in Fig. 15(b). Thus, more than double the displacement must be applied in the stage of Fig. 15(c) to increase the phase field value ϕ in the holed plate's right location to, finally, crack the whole plate in Fig. 15(d).

The effect of the holes is clearly observed in the load displacement curves presented in Fig. 16 for different CNT volume fractions. Firstly, the curves rise similarly to the place in traction in Section 4.2.1 until reaching a maximum traction force. Afterwards, the load bearing capacity rapidly decreases until achieving a second stable region where small displacements occur due to the change of the direction of the crack from completely straight to be bent towards the bottom edge. Is wort noting that considerable larger displacements must be applied to reach a second critical displacement until the crack crosses completely the plate.

Similarly to the previous case studies, higher CNT contents lead to larger fracture energies and Young's moduli of the resulting composite, leading to higher load bearing capacities and larger slopes of the force-displacement curves in the elastic region. For instance, a CNT volume fraction of 2% leads to a load bearing capacity of 6

kN, almost the double capacity of the plate made of pristine epoxy. Also, the force that the thin plate can bear is substantially decreased by the CNTs agglomeration.

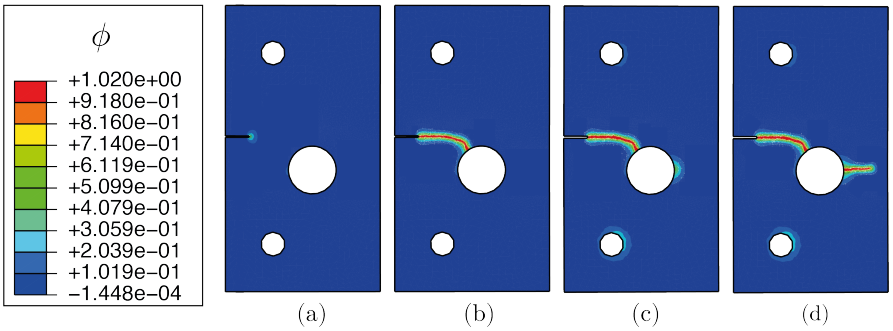

Figure 15: Phase field contour plots (ϕ) in a holed plate under traction for different imposed displacements, namely (a) u_y = 0.104 mm, (b) u_y = 0.106 mm, (c) u_y = 0.299 mm, (d) u_y = 0.320 mm, for a volume fraction of 1% of uniformly dispersed CNTs.

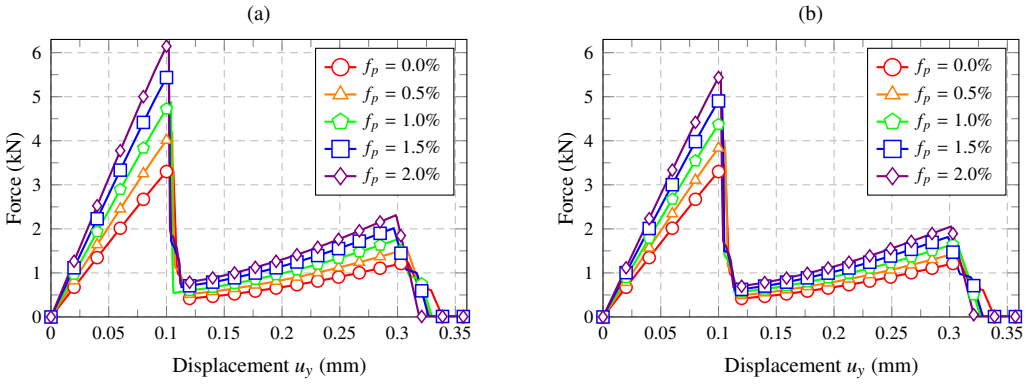

Figure 16: Notched specimen with a hole displacement curve trough volume fractions, for well-dispersed (a) and agglomerated CNTs (b). For the inhomogeneous case the parameters shown in Table. 2.

5. Conclusions

This paper has presented a micromechanical-based approach to estimate the mechanical properties of CNT-based composites, introducing a novel agglomeration model for the fracture energy. The estimates of the elastic and fracture energy are introduced into phase field FEM model to predict the crack growth and propagation throughout macrostructural elements. In order to demonstrate the potentials of the proposed approach, four case studies of full-scale MWCNT/epoxy structural system have been presented. The analyses have appraised the effects of the main microstructural aspect (filler aspect ratio, volume fraction, and filler agglomeration) upon the macroscopic fracture behaviour. The key main findings of this work can be summarised as follows:

- An increase in CNT filler in the composite has improved the overall mechanical properties, considering uniformly dispersed and agglomerated CNTs.
- The agglomeration model to include inhomogeneous dispersions of fillers severely penalises the elastic moduli and the fracture energy.

- The introduction of the CNTs orientation as a parameter in the model provides a conservative value of the mechanical properties.
- As more CNTs filler are added to the composite, more force can resist the thin plate before cracking; however, the displacement increase is neglected because the CNTs also enhanced the elastic moduli, increasing the fracture energy.

References

[1] T. Hassan, A. Salam, A. Khan, S. U. Khan, H. Khanzada, M. Wasim, M. Q. Khan, I. S. Kim, Functional nanocomposites and their potential applications: A review, Journal of Polymer Research 28 (2) (2021) 1–22.

[2] A. M. Esawi, M. M. Farag, Carbon nanotube reinforced composites: Potential and current challenges, Materials Design 28 (9) (2007) 2394–2401.

[3] S. R. Bakshi, D. Lahiri, A. Agarwal, Carbon nanotube reinforced metal matrix composites - a review, International Materials Reviews 55 (1) (2010) 41–64.

[4] J. Wang, X. Deng, S. Du, F. Cheng, F. Li, L. Lu, H. Zhang, Carbon nanotube reinforced ceramic composites: A review, Interceram - International Ceramic Review 63 (6) (2014) 286–289.

[5] M. Zhou, Z. Wang, X. Wang, Carbon nanotubes for sensing applications, in: Industrial applications of carbon nanotubes, Elsevier, 2017, pp. 129–150.

[6] E. García-Macías, A. D'Alessandro, R. Castro-Triguero, D. Pérez-Mira, F. Ubertini, Micromechanics modeling of the uniaxial strain-sensing property of carbon nanotube cement-matrix composites for SHM applications, Composite Structures 163 (2017) 195–215.

[7] S. Abdalla, F. Al-Marzouki, A. A. Al-Ghamdi, A. Abdel-Daiem, Different technical applications of carbon nanotubes, Nanoscale research letters 10 (1) (2015) 1–10.

[8] B. I. Yakobson, P. Avouris, Mechanical properties of carbon nanotubes, Carbon nanotubes (2001) 287–327.

[9] B. G. Demczyk, Y. M. Wang, J. Cumings, M. Hetman, W. Han, A. Zettl, R. Ritchie, Direct mechanical measurement of the tensile strength and elastic modulus of multiwalled carbon nanotubes, Materials Science and Engineering: A 334 (1-2) (2002) 173–178.

[10] T. Ebbesen, H. Lezec, H. Hiura, J. Bennett, H. Ghaemi, T. Thio, Electrical conductivity of individual carbon nanotubes, Nature 382 (6586) (1996) 54–56.

[11] E. T. Thostenson, Z. Ren, T. W. Chou, Advances in the science and technology of carbon nanotubes and their composites: a review, Composites Science and Technology 61 (13) (2001) 1899–1912.

[12] M. Hori, S. Nemat-Nasser, Double-inclusion model and overall moduli of multi-phase composites, Mechanics of Materials 14 (3) (1993) 189–206.

[13] E. García-Macías, R. Castro-Triguero, F. Ubertini, Two-step hierarchical micromechanics model of partially saturated porous composites doped with ellipsoidal particles with interface effects, Composites Part B: Engineering 148 (2018) 49–60.

[14] K. Wang, Y. Lu, Y. Rao, N. Wei, J. Ban, Y. Peng, S. Yao, S. Ahzi, New insights into the synergistic influence of voids and interphase characteristics on effective properties of unidirectional composites, Composite Structures 255 (2021) 112862.

[15] T. P. Fries, T. Belytschko, The extended/generalized finite element method: An overview of the method and its applications, International Journal for Numerical Methods in Engineering 84 (3) (2010) 253–304.

[16] X. P. Xu, A. Needleman, Numerical simulations of fast crack growth in brittle solids, Journal of the Mechanics and Physics of Solids 42 (9) (1994) 1397–1434.

[17] M. Ortiz, A. Pandolfi, Finite-deformation irreversible cohesive elements for three-dimensional crack-propagation analysis, International Journal for Numerical Methods in Engineering 44 (9) (1999) 1267–1282.

[18] J. Oliver, A. E. Huespe, S. Blanco, D. L. Linero, Stability and robustness issues in numerical modeling of material failure with the strong discontinuity approach, Computer Methods in Applied Mechanics and Engineering 195 (52) (2006) 7093–7114.

[19] N. Moës, J. Dolbow, T. Belytschko, A finite element method for crack growth without remeshing, International journal for numerical methods in engineering 46 (1) (1999) 131–150.

[20] C. Miehe, M. Hofacker, F. Welschinger, A phase field model for rate-independent crack propagation: Robust algorithmic implementation based on operator splits, Computer Methods in Applied Mechanics and Engineering 199 (45) (2010) 2765–2778.

[21] C. Miehe, F. Welschinger, M. Hofacker, Thermodynamically consistent phase-field models of fracture: Variational principles and multi-field FE implementations, International Journal for Numerical Methods in Engineering 83 (10) (2010) 1273–1311.

[22] M. J. Borden, C. V. Verhoosel, M. A. Scott, T. J. Hughes, C. M. Landis, A phase-field description of dynamic brittle fracture, Computer Methods in Applied Mechanics and Engineering 217-220 (2012) 77–95.

[23] M. J. Borden, T. J. R. Hughes, C. M. Landis, A. Anvari, I. J. Lee, A phase-field formulation for fracture in ductile materials: Finite deformation balance law derivation, plastic degradation, and stress triaxiality effects, Computer Methods in Applied Mechanics and Engineering 312 (2016) 130–166.

[24] E. Martínez-Pañeda, A. Golahmar, C. F. Niordson, A phase field formulation for hydrogen assisted cracking, Computer Methods in Applied Mechanics and Engineering 342 (2018) 742–761.

[25] W. Tan, E. Martínez-Pañeda, Phase field predictions of microscopic fracture and r-curve behaviour of fibre-reinforced composites, Composites Science and Technology 202 (2021) 108539.

[26] Hirshikesh, S. Natarajan, R. K. Annabattula, E. Martínez-Pañeda, Phase field modelling of crack propagation in functionally graded materials, Composites Part B: Engineering 169 (2019) 239–248.

[27] J.-K. Kim, Y. wing Mai, High strength, high fracture toughness fibre composites with interface control—a review, Composites Science and Technology 41 (4) (1991) 333–378.

[28] B. Lauke, W. Pompe, Fracture toughness of short-fibre reinforced thermoplastics, Composites Science and Technology 26 (1) (1986) 37–57.

[29] R. C. Wetherhold, L. K. Jain, The toughness of brittle matrix composites reinforced with discontinuous fibers, Materials Science and Engineering: A 151 (2) (1992) 169–177.

[30] F. H. Gojny, M. H. Wichmann, B. Fiedler, K. Schulte, Influence of different carbon nanotubes on the mechanical properties of epoxy matrix composites–a comparative study, Composites Science and Technology 65 (15-16) (2005) 2300–2313.

[31] L. Jain, R. Wetherhold, Effect of fiber orientation on the fracture toughness of brittle matrix composites, Acta Metallurgica et Materialia 40 (6) (1992) 1135–1143.

[32] S. Y. Fu, B. Lauke, The fibre pull-out energy of misaligned short fibre composites, Journal of materials science 32 (8) (1997) 1985–1993.

[33] C. Menna, C. E. Bakis, A. Prota, Effect of nanofiller length and orientation distributions on mode i fracture toughness of unidirectional fiber composites, Journal of Composite Materials 50 (10) (2016) 1331–1352.

[34] V. Mirjalili, P. Hubert, Modelling of the carbon nanotube bridging effect on the toughening of polymers and experimental verification, Composites Science and Technology 70 (10) (2010) 1537–1543.

[35] A. Negi, G. Bhardwaj, J. S. Saini, K. Khanna, R. K. Godara, Analysis of CNT reinforced polymer nanocomposite plate in the presence of discontinuities using XFEM, Theoretical and Applied Fracture Mechanics 103 (2019) 102292.

[36] T. Vu-Khanh, J. Denault, P. Habib, A. Low, The effects of injection molding on the mechanical behavior of long-fiber reinforced pbt/pet blends, Composites Science and Technology 40 (4) (1991) 423–435.

[37] P. Hine, N. Davidson, R. Duckett, I. Ward, Measuring the fibre orientation and modelling the elastic properties of injection-moulded long-glass-fibre-reinforced nylon, Composites Science and Technology 53 (2) (1995) 125–131, mesostructures and Mesomechanics in Fibre Composites.

[38] R. Von Turkovich, L. Erwin, Fiber fracture in reinforced thermoplastic processing, Polymer Engineering & Science 23 (13) (1983) 743–749.

[39] D. L. Shi, X. Q. Feng, Y. Y. Huang, K. C. Hwang, H. Gao, The Effect of Nanotube Waviness and Agglomeration on the Elastic Property of Carbon Nanotube-Reinforced Composites , Journal of Engineering Materials and Technology 126 (3) (2004) 250–257.

[40] E. García-Macías, A. D'Alessandro, R. Castro-Triguero, D. Pérez-Mira, F. Ubertini, Micromechanics modeling of the electrical conductivity of carbon nanotube cement-matrix composites, Composites Part B: Engineering 108 (2017) 451–469.

[41] J. M. Wernik, S. A. Meguid, Recent Developments in Multifunctional Nanocomposites Using Carbon Nanotubes, Applied Mechanics Reviews 63 (5), 050801 (02 2011).

[42] A. Allaoui, S. Bai, H. Cheng, J. Bai, Mechanical and electrical properties of a mwnt/epoxy composite, Composites Science and Technology 62 (15) (2002) 1993–1998.

[43] G. Gkikas, A. S. Paipetis, Optimisation and analysis of the reinforcement effect of carbon nanotubes in a typical matrix system, Meccanica 50 (2) (2015) 461–478.

[44] D. L. Shi, X. Q. Feng, Y. Y. Huang, K. C. Hwang, H. Gao, The Effect of Nanotube Waviness and Agglomeration on the Elastic Property of Carbon Nanotube-Reinforced Composites , Journal of Engineering Materials and Technology 126 (3) (2004) 250–257.

[45] T. H. Hsieh, A. J. Kinloch, A. C. Taylor, I. A. Kinloch, The effect of carbon nanotubes on the fracture toughness and fatigue performance of a thermosetting epoxy polymer, Journal of Materials Science 46 (23) (2011) 7525–7535.

[46] A. Zeinedini, M. M. Shokrieh, A. Ebrahimi, The effect of agglomeration on the fracture toughness of cnts-reinforced nanocomposites, Theoretical and Applied Fracture Mechanics 94 (2018) 84–94.

[47] W. Xu, F. Wu, Y. Jiao, M. Liu, A general micromechanical framework of effective moduli for the design of nonspherical nano-and micro-particle reinforced composites with interface properties, Materials & Design 127 (2017) 162–172.

[48] W. Xu, H. Ma, S. Ji, H. Chen, Analytical effective elastic properties of particulate composites with soft interfaces around anisotropic particles, Composites Science and Technology 129 (2016) 10–18.

[49] J. K. Beddow, Particle Characterization in Technology: Volume II: Morphological Analysis, CRC press, 2018.

[50] T. Mori, K. Tanaka, Average stress in matrix and average elastic energy of materials with misfitting inclusions, Acta metallurgica 21 (5) (1973) 571–574.

[51] S. Y. Fu, B. Lauke, Effects of fiber length and fiber orientation distributions on the tensile strength of short-fiber-reinforced polymers, Composites Science and Technology 56 (10) (1996) 1179–1190.

[52] V. C. Li, Y. Wang, S. Backer, A micromechanical model of tension-softening and bridging toughening of short random fiber reinforced brittle matrix composites, Journal of the Mechanics and Physics of Solids 39 (5) (1991) 607–625.

[53] M. Piggott, Toughness in obliquely-stressed fibrous composites, Journal of the Mechanics and Physics of Solids 22 (6) (1974) 457–458.

[54] L. Jain, R. Wetherhold, Effect of fiber orientation on the fracture toughness of brittle matrix composites, Acta metallurgica et materialia 40 (6) (1992) 1135–1143.

[55] S. G. Advani, C. L. Tucker III, The use of tensors to describe and predict fiber orientation in short fiber composites, Journal of rheology 31 (8) (1987) 751–784.

[56] M. Xia, H. Hamada, Z. Maekawa, Flexural stiffness of injection molded glass fiber reinforced thermoplastics, International Polymer Processing 10 (1) (1995) 74–81.

[57] F. Gojny, M. Wichmann, U. Köpke, B. Fiedler, K. Schulte, Carbon nanotube-reinforced epoxy-composites: enhanced stiffness and fracture toughness at low nanotube content, Composites science and technology 64 (15) (2004) 2363–2371.

[58] E. Specht, The best known packings of equal circles in a circle, WEB site:¡ http://www. packomania. com¿. Accessed (2014).

[59] E. García-Macías, L. Rodríguez-Tembleque, A. Sáez, MWCNT/epoxy strip-like sensors for buckling detection in beam-like structures, Thin-Walled Structures 133 (2018) 27–41.

[60] A. Anvari, The influence of CNT structural parameters on the properties of CNT and CNT-reinforced epoxy, International Journal of Aerospace Engineering 2020 (2020).